Analytical modeling and optimization of electret-based microgenerators under sinusoidal excitations

Cuong C. Nguyen*†, Damith C. Ranasinghe†, and Said F. Al-Sarawi*

Submitted on February 25th, 2017

Abstract

Small scale electrostatic energy harvesters or microgenerators have attracted much interest due to their compatibility with micro-electro-mechanical-system (MEMS) fabrication processes and the possibility to energize wireless sensors and actuators through harvesting movement or vibration from surrounding environment. Several analytical models have been developed to estimate the performance of electret-based microgenerators. However, most of these studies focused on constant-speed rotations, while in practice, mechanical stimuli resemble sinusoidal vibrations. Consequently, a combination of finite element modeling and numerical methods has been the primary approach to analyze and optimize the performance of electret-based microgenerators. Both approaches are time-consuming, costly and more importantly, limit the understanding of design trade-offs involved. In this paper, we present an analytical model that accurately predicts the output voltage and effective power generated by electret-based microgenerators under small sinusoidal excitations. The developed model is validated using numerical simulations that show a good agreement with measured results published in the literature. We also employ the analytical model to optimize the microgenerator by investigating the effects of electret thickness, air gap spacing between the two plates of the microgenerator, and electret surface potential with respect to material properties.

1 Introduction

The rapid growth of Internet-of-Things applications is driving innovations in the field of energy harvesting to enable the capabilities of autonomous sensing and monitoring. During the last decade, a significant number of micro-scale vibratory energy harvesters has been fabricated using active materials (piezoelectric (Sodano et al. 2004, Roundy & Wright 2004), ferroelectric (Asanuma et al. 2013) and magnetoelectric (Zhou et al. 2013)) or exploiting the electromechanical coupling mechanisms (electromagnetic (Williams & Yates 1996, James et al. 2004, Romero et al. 2009) and electrostatic (Meninger et al.

*Centre for Biomedical Engineering, School of Electrical and Electronic Engineering, University of Adelaide, South Australia, Australia 5005

†Auto-ID lab, School of Computer Science, University of Adelaide, South Australia, Australia 5005

2001, Yen & Lang 2006, Boisseau et al. 2011)) to harvest energy from mechanical stimuli or ambient vibrations. Such transduction mechanisms have both benefits and limitations that vary depending on the employed technology and the targeted application. For miniaturization, electrostatic systems are favorable due to their compatibility with MEMS fabrication processes. In addition, electrostatic systems with pre-charged electrets can autonomously harvest energy to energize microelectronic devices such as wireless sensors and actuators.

Electret-based microgenerators had been well studied and developed even before the era of micro- and nano-technologies. Significant early research efforts on electret generators were undertaken by Jefimenko & Walker (1978) and Tada (1986, 1992). Later, Boland et al. (2003) employed advances in micromachining to prototype a cross-wafer connected electret-based microgenerator with both the electrets and counter electrodes patterned, as illustrated in Figure 1, and derived a theoretical model to estimate the output voltage and power generated under constant-speed rotations. Subsequently, several studies implemented the theoretical model to design and optimize the performance of microgenerators ((Tsutsumino, Suzuki, Kasagi & Sakane 2006, Naruse et al. 2009, Masaki et al. 2011, Chen & Suzuki 2013, Nakano et al. 2015)). Bartsch et al. (2009) further extended Boland et al.'s model by taking parasitic capacitance effect into account to accurately predict both voltage and power at the output. However, these theoretical studies were all taken under constant-speed rotations, while vibrations, in reality, resemble sinusoidal forms. Consequently, a combination of extensive finite element modeling and numerical methods has been the primary approach to investigate and design electret-based microgenerators under sinusoidal excitation. Both approaches are time-consuming, costly and more importantly, limit the understanding of design trade-offs.

In this paper, we develop an analytical model which can accurately predict the output voltage and power generated by electret-based microgenerators under small sinusoidal excitations. We employ the analytical model to investigate the optimization of electret-based microgenerators under practical limitations imposed by material properties.

The remainder of the paper is organized as follows: section 2 presents the formulation of theoretical model using linear circuit elements. Parasitic capacitances are also taken into account to refine the theoretical model for accurate prediction. Section 3 describes a finite element modeling (FEM) to compute the microgenerator capacitance, including stray fields and presents a numerical-based simulation that employs the FEM results to calculate output voltage and power generated by the microgenerator. In section 4, the time average power and output voltage calculated using the analytical model is validated. Section 5 takes the effects of voltage breakdown into account and combines with the analytical model to optimize the performance of electret-based microgenerators.

2 Theory development

2.1 Theoretical model

Boland et al. (2003) derived the governing equation that correlated the rate of change of charge induced on counter electrodes to the relative movement of electret-based cross-wafer microgenerators, illustrated in Figure 1, as

$$\frac{dQ(t)}{dt} = -\left[\frac{Q(t)}{R_L C_0}\frac{A_0}{A(t)} + \frac{V_0}{R_L}\right], \tag{1}$$

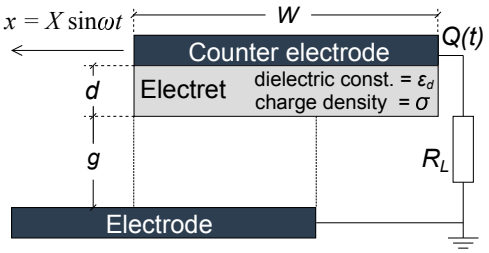

Figure 1. Illustration of an electret-based cross-wafer microgenerator.

where A_0 is the maximum overlapping area, C_0 is the maximum capacitance and V_0 is the surface potential of the electret. Both C_0 and V_0 are defined as

$$C_0 = \frac{\varepsilon_d \varepsilon_0 A_0}{d + \varepsilon_d g} \quad \text{and} \quad V_0 = \frac{\sigma d}{\varepsilon_d \varepsilon_0}.$$

The induced charge $Q(t)$ in equation (1) relies on the time variant overlapping area $A(t)$, which depends on the type of the excitation. For a constant-speed rotations, the overlapping area $A(t)$ is a linear function of time. This equation can, therefore, be solved easily for a closed-form solution, while the situation is different for a sinusoidal function. Under a small sinusoidal excitation $x = X \sin \omega t$, where the amplitude X is smaller than the electrode width, W, the overlapping area is defined as

$$A(t) = kA_0 |\sin \omega t| \qquad \text{where } k = \frac{X}{W} \leq 1. \tag{2}$$

The harmonic non-linear term associated with the overlapping $A(t)$ complicates the integration of the equation (1) and consequently, places a roadblock that prevents obtaining an analytical solution of the induced charge $Q(t)$. To overcome this difficulty, we approximate the sinusoidal function in (2) to a parabolic function expressed by

$$A(t) \approx kA_0 \frac{4\omega t}{\pi} \left(1 - \frac{\omega t}{\pi}\right). \tag{3}$$

The dimensionless comparison between the two functions plotted in Figure 2 shows that the parabolic function can accurately approximate the sinusoidal variation of the overlapping area. In addition to simplify the analysis, the symmetry of the structure and the periodic nature of the excitation are utilized, so that, only the first half cycle of the vibration is investigated. Within this period, equation (1) is rewritten as

$$\frac{dQ(t)}{dt} = -\left[\frac{Q(t)}{4kR_L C_0 \frac{\omega t}{\pi}\left(1 - \frac{\omega t}{\pi}\right)} + \frac{V_0}{R_L}\right]. \tag{4}$$

We employ the integrating factor method to solve equation (4). Let $M(t)$ be a function such that

$$M(t) = \int_{\frac{\pi}{2\omega}}^{t} \frac{d\tau}{4kR_L C_0 \frac{\omega\tau}{\pi}\left(1 - \frac{\omega\tau}{\pi}\right)} = \frac{\pi}{4k\omega R_L C_0} \ln\left(\frac{\omega t}{\pi - \omega t}\right). \tag{5}$$

The integrating factor is then defined as

$$\exp\left[M(t)\right] = \exp\left[\frac{\pi}{4k\omega R_L C_0} \ln\left(\frac{\omega t}{\pi - \omega t}\right)\right] = \left(\frac{\omega t}{\pi - \omega t}\right)^{\frac{\pi}{4k\omega R_L C_0}}. \tag{6}$$

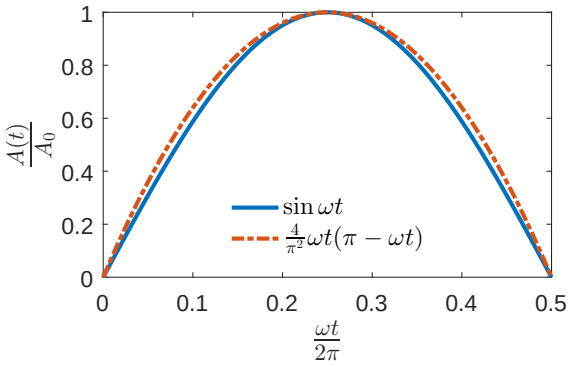

Figure 2. The sinusoidal variation of overlapping area can be approximated well by a parabolic function.

The solution of charge $Q(t)$ induced in the counter electrode of the microgenerator can be expressed by

$$\begin{aligned} Q(t) &= c_1 \exp\left[-M(t)\right] + \exp\left[-M(t)\right] \int_0^t \exp\left[M(\tau)\right] \left(-\frac{V_0}{R_L}\right) d\tau \\ &= c_1 \left(\frac{\pi - \omega t}{\omega t}\right)^{\frac{\pi}{4k\omega R_L C_0}} - \frac{V_0}{R_L} \left(\frac{\pi - \omega t}{\omega t}\right)^{\frac{\pi}{4k\omega R_L C_0}} \underbrace{\int_0^t \left(\frac{\omega \tau}{\pi - \omega \tau}\right)^{\frac{\pi}{4k\omega R_L C_0}} d\tau}_{N(t)} . \end{aligned} \tag{7}$$

Comparing with the results derived for a constant-speed rotation, the nonlinearity of the parabolic-profile overlapping area leads to the complicated integral $N(t)$ presented in (7). According to the result (3.194-1) given in (Gradshteyn & Ryzhik 2014), $N(t)$ can be presented using a hypergeometric function ${}_2\mathrm{F}_1(a, b; c; z)$. Hypergeometric functions are a generalization of exponential functions that cannot be explicitly presented using elementary mathematical functions. However, the functions are well studied in the literature and can also be manipulated analytically. In this paper, we employ some derived properties of the functions to simplify and linearize the solution of equation (4) for further analysis.

We employ the result (3.194-1) in (Gradshteyn & Ryzhik 2014) to rewrite $N(t)$ as

$$\begin{aligned} N(t) = &\frac{\pi}{\omega\left(1 + \frac{\pi}{4k\omega R_L C_0}\right)} \left(\frac{\omega t}{\pi}\right)^{1 + \frac{\pi}{4k\omega R_L C_0}} \\ &\times {}_2\mathrm{F}_1\left(\frac{\pi}{4k\omega R_L C_0}, 1 + \frac{\pi}{4k\omega R_L C_0}; 2 + \frac{\pi}{4k\omega R_L C_0}; \frac{\omega t}{\pi}\right) . \end{aligned} \tag{8}$$

We then use the Euler's transform of the hypergeometric function presented in (Weisstein 2002) to simplify further $N(t)$

$$\begin{aligned} N(t) = &\frac{\pi}{\omega\left(1 + \frac{\pi}{4k\omega R_L C_0}\right)} \left(\frac{\omega t}{\pi}\right)^{1 + \frac{\pi}{4k\omega R_L C_0}} \left(1 - \frac{\omega t}{\pi}\right)^{1 - \frac{\pi}{4k\omega R_L C_0}} \\ &\times {}_2\mathrm{F}_1\left(1, 2; 2 + \frac{\pi}{4k\omega R_L C_0}; \frac{\omega t}{\pi}\right) . \end{aligned} \tag{9}$$

Given $N(t)$ in (9), the solution of the charge $Q(t)$ in (7) can be expressed by

$$Q(t) = c_1 \left(\frac{\pi - \omega t}{\omega t}\right)^{\frac{\pi}{4k\omega R_L C_0}} - \frac{4k\omega C_0 V_0 t}{4k\omega R_L C_0 + \pi}\left(1 - \frac{\omega t}{\pi}\right) {}_2\mathrm{F}_1\left(1, 2; 2 + \frac{\pi}{4k\omega R_L C_0}; \frac{\omega t}{\pi}\right). \tag{10}$$

At time $t = 0$, there is no overlap between the two plates of the microgenerator, the induced charge $Q(0) = 0$, and therefore $c_1 = 0$. Here, it is more useful to consider the series expansion of the hypergeometric function specified in (Weisstein 2002) and express $Q(t)$ as

$$\begin{aligned} Q(t) &= -\frac{4k\omega C_0 V_0 t}{4k\omega R_L C_0 + \pi}\left(1 - \frac{\omega t}{\pi}\right) \times {}_2\mathrm{F}_1\left(1, 2; 2 + \frac{\pi}{4k\omega R_L C_0}; \frac{\omega t}{\pi}\right) \\ &= -\frac{4k\omega C_0 V_0 t}{4k\omega R_L C_0 + \pi}\left(1 - \frac{\omega t}{\pi}\right) \times \left(1 + \frac{8k\omega R_L C_0}{8k\omega R_L C_0 + \pi}\frac{\omega t}{\pi} + \dots\right). \end{aligned} \tag{11}$$

For the applications of practical microgenerators, the maximum capacitance C_0 is only a few pF due to the micro scale of the generators, and the external load R_L varies in the range of MΩ. As a result, the value of $R_L C_0$ is very small (less than 10^{-5} s). In addition, the target of vibration energy harvesting is at low frequencies such as electrical powered machines (60 - 120 Hz (Roundy et al. 2003)), human (less than 2.5 Hz (Hirasaki et al. 1999)) or animal motions (less than 3 Hz for sharks (Graham et al. 1990)). It is also worthy to note that k is less than or equals to 1. We can, therefore, employ the assumption of a very small $k\omega R_L C_0$ to approximate the hypergeometric function to the lowest order term and obtain the closed-form solution

$$Q(t) \approx -\frac{4k\omega C_0 V_0 t}{4k\omega R_L C_0 + \pi}\left(1 - \frac{\omega t}{\pi}\right). \tag{12}$$

The current $I(t)$ passing through the external load R_L can be calculated by employing the result obtained in (12) and expressed as

$$I(t) = -\frac{dQ(t)}{dt} = \frac{4k\omega C_0 V_0}{4k\omega R_L C_0 + \pi}\left(1 - \frac{2\omega t}{\pi}\right). \tag{13}$$

The output voltage $V(t)$ generated across the external load R_L between the two terminals of the microgenerator follows Ohm's law and therefore

$$V(t) = R_L\, I(t) = \frac{4k\omega R_L C_0 V_0}{4k\omega R_L C_0 + \pi}\left(1 - \frac{2\omega t}{\pi}\right). \tag{14}$$

We can now employ the results obtained in the formulations of current $I(t)$ and voltage $V(t)$ to model the generator using linear circuit elements. First, we investigate the two important characteristics of a generator: short circuit current and open circuit voltage. The short circuit current is determined as the external load reaches zero

$$I_{\mathrm{sc}}(t) = \lim_{R \to 0} I(t) = \left(1 - \frac{2\omega t}{\pi}\right)\frac{4k\omega C_0 V_0}{\pi}. \tag{15}$$

The open circuit voltage is calculated as the external load R_L approaches infinity, which results in

$$V_{\mathrm{oc}}(t) = \lim_{R \to \infty} V(t) = \left(1 - \frac{2\omega t}{\pi}\right) V_0. \tag{16}$$

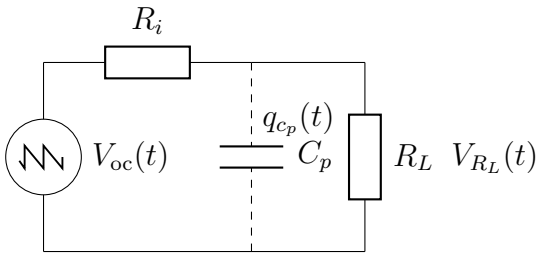

Figure 3. A cross-wafer microgenerator is modeled as a saw-tooth voltage source V_{oc} in series with an internal resistance R_i. Parasitic capacitance C_p is included to refine the model for practical microgenerators.

The derivations in (15) and (16) results in a time independent ratio between the open circuit voltage and short circuit current, which is indeed the characteristic of a resistor. The microgenerator can, therefore, be modeled as a voltage source $V_{\text{oc}}(t)$ in series with an equivalent internal resistor R_i defined as

$$R_i = \frac{V_{\text{oc}}(t)}{I_{\text{sc}}(t)} = \frac{R_0}{8k}, \tag{17}$$

where R_0 is defined as

$$R_0 = \frac{1}{fC_0}, \tag{18}$$

and f is the frequency of the excitation.

Remark. *A similar internal resistance for electret-based microgenerators can also be observed under rotational excitations (Bartsch et al. 2009)*

$$R_{i-\text{rot}} = \frac{R_0}{2n}, \tag{19}$$

where n is the number of microgenerator poles.

R_0 is directly analogous to the equivalent resistance of a switched capacitor C_0 at a switching frequency f as presented in (Franco 2002). Hence, a switched capacitor circuit can be used as an analogy to illustrate the operation mechanism of capacitive microgenerators.

Under constant-speed rotations, Bartsch et al. (2009) employed the result derived by Boland et al. (2003) to model the microgenerator as a constant voltage source in series with an internal resistor. In contrast, we modeled the microgenerator under a small sinusoidal excitation as a saw-tooth voltage source in series with an internal resistor, illustrated in Figure 3. Therefore, the dynamic behaviors of the microgenerator can be presented under the two different forms of excitations as shown in Table 1.

2.2 Influence of parasitic capacitance

Although the theoretical model can be used to guide the designs of electret-based microgenerators, Bartsch et al. (2009) highlight that unavoidable parasitic capacitances affects the performance of the microgenerator, causing discrepancy between modeled and measured performance. To take this capacitance into account, all load capacitances are absorbed into C_p connected in parallel to the external load R_L as shown in Figure 3.

The governing equation of the equivalent circuit in Figure 3, including C_p, describes the current flowing through C_p in term of the charge $q_{c_p}(t)$ stored in C_p

$$\frac{dq_{c_p}(t)}{dt} = \frac{1}{R_i}\left[V_{\text{oc}}(t) - \frac{q_{c_p}(t)}{C_p}\right] - \frac{q_{c_p}(t)}{R_L C_p}. \tag{20}$$

The boundary conditions are based on the periodic nature of the overlapping area which results in

$$q_{c_p}(0) = q_{c_p}\left(\frac{\pi}{\omega}\right). \tag{21}$$

The solution of equation (20) can be obtained analytically in the first half cycle of the excitation. The output voltage across R_L equals to the dropped voltage of C_p and is calculated as

$$V_{R_L}(t) = \frac{q_{c_p}(t)}{C_p} = \left[1 - \frac{2\omega t}{\pi} + \underbrace{\frac{2\omega R_p C_p}{\pi} + \frac{2e^{\frac{-t}{R_p C_p}}}{e^{\frac{-\pi}{\omega R_p C_p}} - 1}}_{\text{parasitic capacitance effect}}\right]\frac{R_L}{R_L + R_i}V_0, \tag{22}$$

where $R_p = R_L \| R_i$.

The effective power of the microgenerator can also be calculated as the average of instantaneous power

$$\begin{aligned} P &= \frac{\omega}{\pi R_L}\int_0^{\frac{\pi}{\omega}} V_{R_L}^2(t)\, dt \\ &= \frac{V_0^2 R_L}{(R_L + R_i)^2}\left[\frac{1}{3} + \frac{2\omega R_p C_p}{\pi} \times \left(\frac{2\omega R_p C_p}{\pi} - \frac{2}{e^{\frac{\pi}{\omega R_p C_p}} - 1} - 1\right)\right]. \end{aligned} \tag{23}$$

3 FEM capacitance and numerical solution

This section presents a FEM computation of capacitance and numerical methods to solve equation (1) for the induced charge $Q(t)$. The solution is then used to numerically calculate the output voltage and time average power of the microgenerator.

The differential equation governing the electrodynamics of the microgenerators in (1) can be rewritten as

$$\frac{dQ(t)}{dt} = -\left[\frac{Q(t)}{R_L C_{\text{FEM}}} + \frac{V_0}{R_L}\right], \tag{24}$$

where C_{FEM} is the computed capacitance using FEM.

Table 1. Analytical model of electret-based microgenerators under rotational and sinusoidal motions.

Excitation type	**Analytical model**	
	Voltage source	Internal resistance
Rotational	V_0	$\frac{R_0}{2n}$
Sinusoidal	$\left(1 - \frac{2\omega t}{\pi}\right)V_0$	$\frac{R_0}{8k}$.

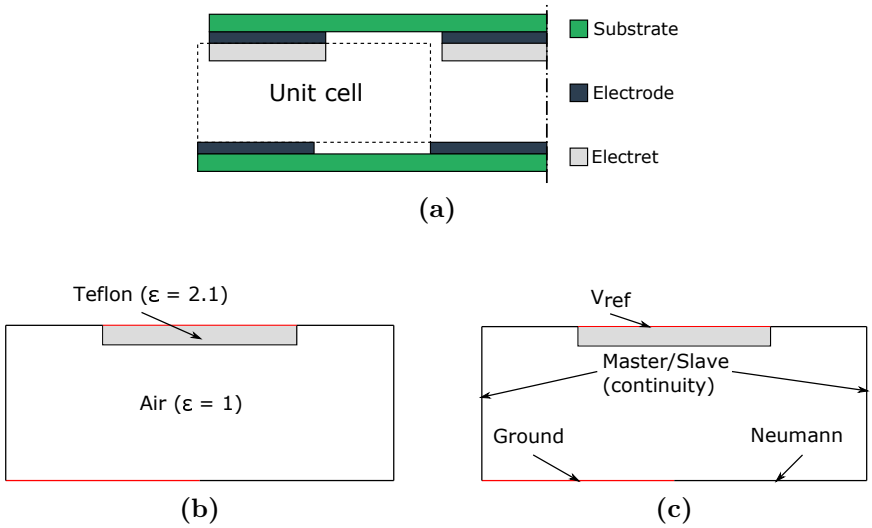

Figure 4. Details of the FEM model: (a) definition of a unit celll, (b) materials used in the FEM simulation and (c) boundary condition setup.

In order to numerically solve equation (24), C_{FEM} must be determined. The Maxwell 2D module of ANSYS Electronics Desktop 2016.1 is employed to calculate C_{FEM} of a unit cell illustrated in Figure 4(a). The materials and boundary conditions used in the FEM model are presented in Figure 4(b) and Figure 4(c). The electrode and counter electrode are considered in the FEM as parts of the boundary conditions. The FEM is carried out by setting a voltage V_{ref} on the counter electrode while grounding the electrode. The counter electrodes are then moved in steps along the horizontal axis. At each step x, the FEM capacitance C_{FEM} is recorded.

The results of C_{FEM} presented in Figure 5 resemble a cosine function of the displacement which agrees with the study that Boisseau et al. conducted on a similar structure in Boisseau et al. (2010). Hence, C_{FEM} can be approximated as

$$C_{\text{FEM}}(x) = \frac{C_{\max} + C_{\min}}{2} + \frac{C_{\max} - C_{\min}}{2} \cos\left(\frac{\pi x}{W} - \pi\right), \tag{25}$$

where $C_{\max}$ and $C_{\min}$ are the maximum and minimum FEM values of capacitance, respectively, and depend on the geometry of the microgenerator.

The expression of the capacitance presented in (25) is consistent with the results reported by Boisseau et al. (2010), with the theoretical overlap area at $x = 0$ defined as 0 percent, while in Boisseau et al. (2010), the theoretical overlap area at $x = 0$ is 100 percent. This difference is purposely designed to ensure the consistency between the FEM based simulation and the assumption made in (12).

Numerical algorithms implemented in MATLAB are then used to solve equation (24) to calculate the output voltage and time average power of the microgenerator. The algorithm operates as the following. First, the input vibration is set as $x = X \sin \omega t$. Second, the expression of FEM capacitance obtained in (25) is inserted into the differential equation (24). The equation is then solved in the time domain for the induced charge $Q(t)$ using a numerical solver. A sub-algorithm is defined to determine when the system reaches steady state. Subsequently, the output voltage of the microgenerator can be calculated as

$$V_{\text{FEM}}(t_n) = -R_L \frac{Q_{\text{FEM}}(t_n) - Q_{\text{FEM}}(t_{n-1})}{t_n - t_{n-1}}. \tag{26}$$

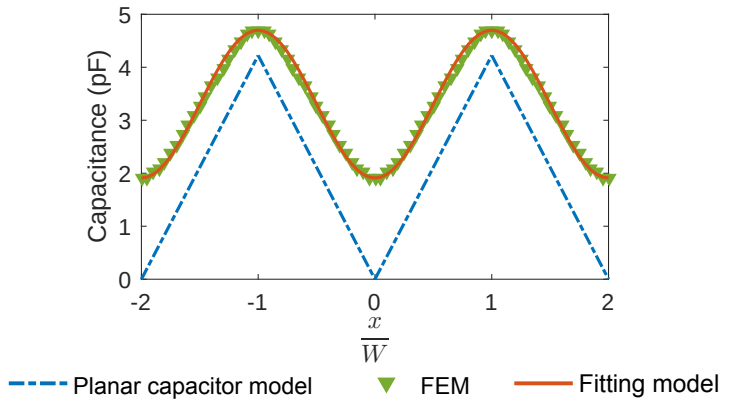

Figure 5. FEM result of capacitance resembles well a sinusoidal function.

The result of $V_{\mathrm{FEM}}(t)$ is then employed to compute the root mean squared (RMS) voltage V_{RMS}. Finally, the time average power dissipated in the external load R_L is calculated using the formula

$$P_{\mathrm{FEM}} = \frac{V_{\mathrm{RMS}}^2}{R}. \tag{27}$$

The procedure is repeated for various values of the external load R_L.

4 Comparison between theory and simulation

The microgenerator reported in (Tsutsumino, Suzuki, Kasagi & Sakane 2006) is employed in this comparison. The device consists of two 20-by-10 mm^2 plates separated by a 200 μm air gap. A 20 μm thick CYTOP with a total area of 100 mm^2 is deposited on 1 mm wide electrodes and then charged to -600 V. The microgenerator is tested under a 2 mm peak-to-peak excitation with several different frequencies. All parameters related to this microgenerator are summarized in Table 2. The output voltage and effective power of the microgenerator calculated employing our formulated solution presented in section 2 is compared with the simulation-based method described in section 3.

In order to evaluate the analytical model, lumped parasitic capacitance C_p of the analytical solution must be determined. C_p can be obtained either by measuring physical devices and harvesting circuits or fitting the analytical model to numerical simulations

Table 2. Parameters used to compare the analytical model and simulation

Parameter	Description	Value
ε_d	Dielectric constant of CYTOP	2.1
n	Number of electrodes	10
W	Width of one electrode	1 mm
L	Out-of-plane length of one electrode	10 mm
d	Electret thickness	20 μm
g	Air gap between two plates	200 μm
V_0	Electret surface potential	600 V
X	Amplitude of excitation	1 mm
f	Forcing frequency	5, 10, 15 and 20 Hz.

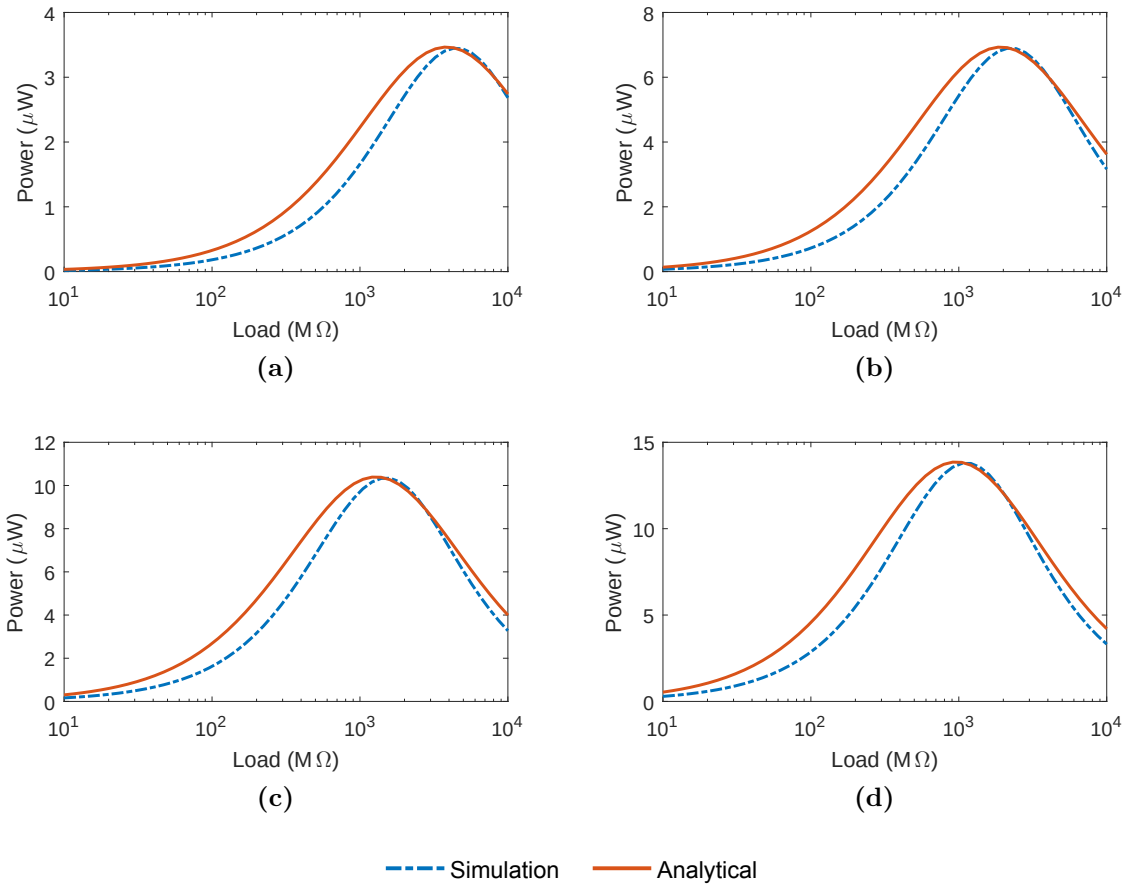

Figure 6. The effective power of the microgenerator predicted by the analytical model and the simulation at four different frequencies: (a) 5 Hz, (b) 10 Hz, (c) 15 Hz and (d) 20 Hz. C_p is evaluated as 2.27 pF.

or experimental data. In this section, we employ the latter approach and obtain a value of 2.27 pF for lumped parasitic capacitance C_p. For the numerical simulation, $C_{\max}$ and $C_{\min}$ are computed as 4.7 pF and 1.9 pF, respectively.

The generated powers of the microgenerator calculated using the closed-form expression in (23) and the numerical simulation are shown in Figure 6. The analytical solutions are in good agreement with the simulation results and in particular the ability to predict the peak power. The discrepancy between the analytical model and numerical simulation is due to the approximation from a pure sinusoid to a parabolic function made in (3). Nevertheless, the analytical model can well predict the effective power and can facilitate the needed understanding of the design trade-offs and ideally optimization, due to the low computational overhead when using full FEM approach.

We further evaluate our model by comparing the calculated output voltage with the simulation. The output voltages plotted in Figure 7 at 10 MΩ and 500 MΩ shows an adequate prediction of the peak-to-peak voltages. The difference between the cotangent-like shape of simulated signal and the straightline response of our model is due to the approximation made in (3). Another discrepancy is the sharp peaks of the analytical model as highlighted in both sub figures of Figure 7. This error is due to the non-differentiation of the theoretical overlapping area that occurs at every half cycle. As highlighted in Figure 8, the overlapping area defined in (3) is non-differentiable when

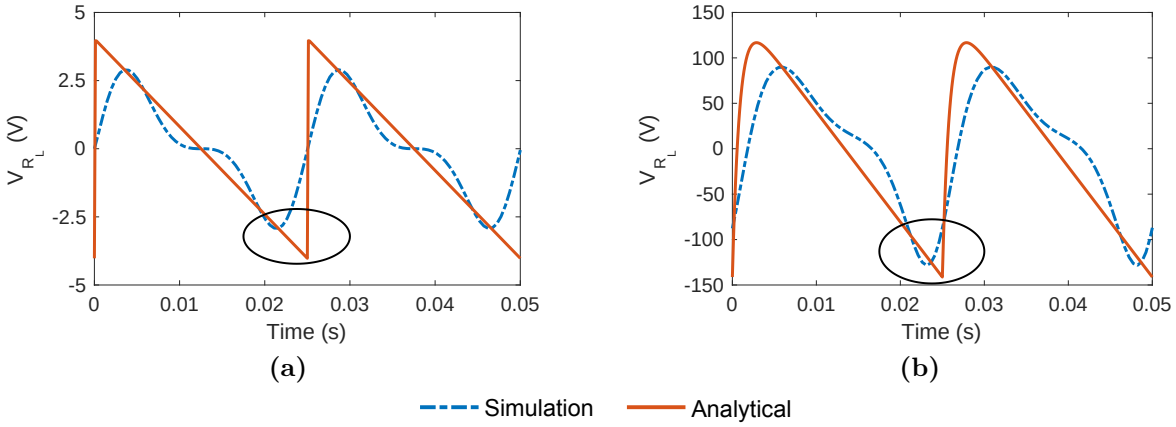

Figure 7. The output voltage of the microgenerator predicted by the analytical model and the simulation under two different loads: (a) 10 MΩ and (b) 500 MΩ at 20 Hz excitation. The shapes of the calculated and simulated signals are different due to the approximation of instantaneous overlapping area from a sinusoid to a parabolic function.

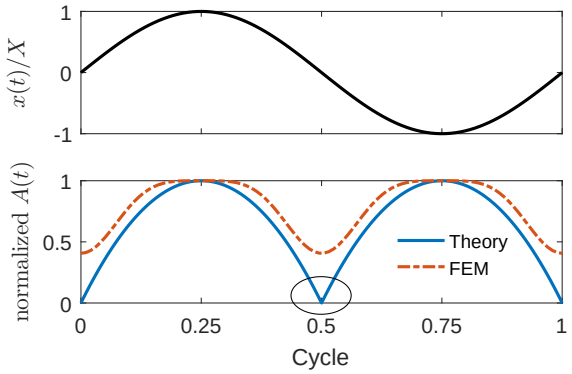

Figure 8. Theoretical overlapping area is non-differentiable when the counter electrode crosses origin, while the FEM overlapping area derived from C_{FEM} is a smooth curve. This factor attributes to the sharp peaks observed in the analytical output voltage presented in Figure 7.

the counter electrode crosses the origin point ($x = 0$), while the FEM overlapping area derived from C_{FEM} is differentiable everywhere in the time domain. The consequence of that non-differentiation causes spike shapes between the two half cycles in our model, comparing with rounded peaks in the FEM simulation.

Even though the non-linear electrodynamics of cross-wafer microgenerators under sinusoidal vibration complicates the analysis and prevents obtaining precise results, the presented model allows the prediction of the microgenerator performance with reasonable accuracy, especially output power estimation. In the next section, we employ the proposed model to investigate design parameter influence on the performance of the electret-based microgenerators.

5 Optimization strategy

The common approaches to improve electret-based microgenerator performance are to: (i) increase the overlapping area A_0; (ii) decrease the thickness d of the electret; or (iii)

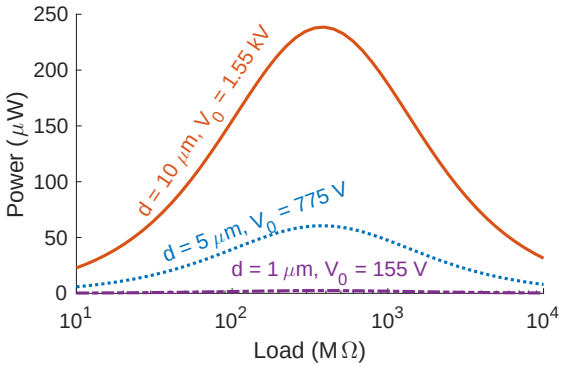

Figure 9. Various thicknesses of the electret and surface potentials corresponding to the dielectric strength are used to calculate the output power of the microgenerator. Owing to the limitation of internal breakdown effect, reducing the thickness of electret does not always improve the output power.

reduce the air gap distance g between the two plates of the microgenerator. While a larger A_0 results in a larger device, reducing d or g is desirable since that can further shrink down the microgenerator volume. However, excessive reduction of d or g can be problematic due to the limitation of material breakdown caused by the electret's high surface potential voltage, V_0.

In this section, we employ the analytical model developed in section 2 to optimize the performance of the electret-based microgenerator described in Table 2 with respect to the electret thickness d, the air gap spacing g, and the electret surface potential V_0 under practical limitations imposed by material properties.

Depending on the dielectric strength of electret material, reducing d can lead to the occurrences of internal breakdown. For example, the dielectric strength of Teflon PTFE, a widely used material to make electret, is about 155-200 MV/m (Smith 2013) which imposes a 155 V limit when using a 1-μm-thick film. Figure 9 plots the output power with various values of Teflon PTFE thickness and the corresponding breakdown voltage. Based on the result, decreasing the thickness d of the electret beyond a specific value might not result in an improvement. However, using a too thick electret film is also unfavorable since it would bring down the performance of the microgenerator. For a thin electret, Genter & Paul (2012) reported that a smaller d exacerbates charge decay. Based on their experimental result, a thickness between 11 - 23 μm was recommended to ensure charge stability while still obtaining a decent surface potential.

Reducing g also leads to another breakdown as described in Paschen's law. One example of external voltage breakdown in electret-based microgenerators was observed in (Tsutsumino, Suzuki, Kasagi & Sakane 2006) when a -950V pre-charged electret was employed to assemble a microgenerator with 100 μm air gap. According to Paschen's law for air at atmospheric pressure as presented in Figure 10, a maximum voltage difference of 785.9 V can be used at $g = 100$ μm to avoid the external breakdown (Husain & Nema 1982). Consequently, the surface potential of the electret in (Tsutsumino, Suzuki, Kasagi & Sakane 2006) was reported to drop to -400 V. One solution is to fill the gap with different dielectric media that has higher Paschen's discharge voltage such as vacuum or insulating gas (SF_6 in (Tsutsumino, Suzuki, Kasagi, Kashiwagi & Morizawa 2006)). The downside of this method is to complicate the packaging process, resulting in a higher cost and defect rate. Nevertheless, air is still a preferable dielectric media due to simplicity

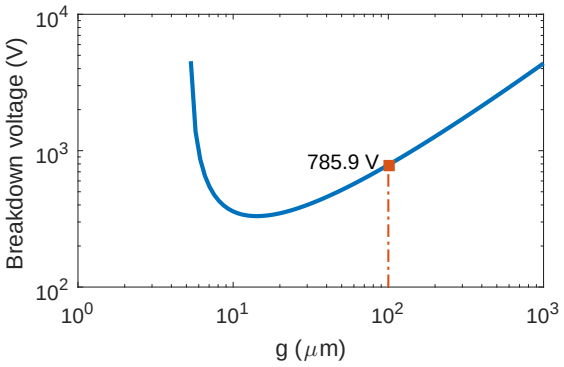

Figure 10. Breakdown voltage of air at atmospheric pressure. Data is taken from (Husain & Nema 1982).

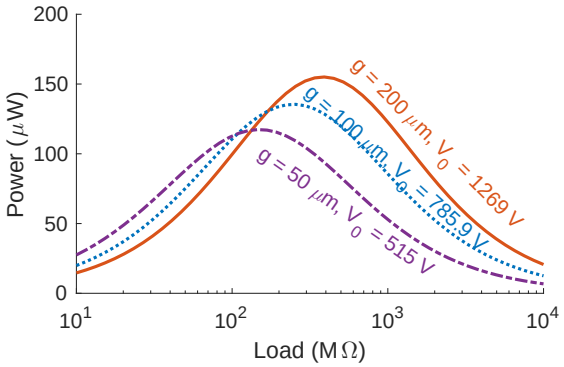

Figure 11. Various air gap distances and their corresponding Paschen's breakdown voltage are used to calculate the output power of the microgenerator. By including the effect of voltage breakdown, reducing g does not always result in a better performance.

and economy .

Considering the effect of voltage breakdown on the microgenerator performance, we calculate the output power generated by the electret-based microgenerator with different values of g and the corresponding maximum allowable voltage according to Paschen's law and show the result in Figure 11. The results show that a smaller g does not lead to a higher power generation. Hence, voltage breakdown effects should be considered carefully when designing and optimizing electret-based microgenerators.

By considering the dielectric strength of materials and voltage breakdown effects, the optimization of an electret-based microgenerator becomes a constrained non-linear multi-variable problem expressed as

$$\max P \text{ such that } \begin{cases} 0 < V_0 \leq V_{\max} \\ d_{\min} \leq d \leq d_{\max} \\ g_{\min} \leq g \leq g_{\max} \\ R_{\min} \leq R_L \leq R_{\max} \\ V_0 \leq E_0\, d \\ V_0 \leq V_p(g) \\ f = f_0 \end{cases}, \tag{28}$$

where $V_{\max}$ is the maximum voltage that can be used to charge the electret, $d_{\min}$, $d_{\max}$,

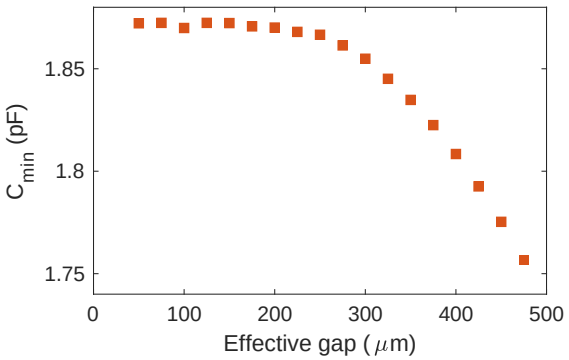

Figure 12. The variation of the minumum FEM capacitance $C_{\min}$ is insignificant (less than 0.15 pF) for various values of effective gap spacing $d/\varepsilon_d + g$.

$g_{\min}$, $g_{\max}$, $R_{\min}$ and $R_{\max}$ are the lower and upper limits of electret thichkness, air gap spacing between the two plates of the microgenerator and the external load, respectively, E_0 is the dielectric strength of the electret material and $V_p(g)$ is a function that describes the correlation between the external breakdown voltage and the air gap g according to Paschen's law (Husain & Nema 1982).

For practical applications of electret-based microgenerators, $d_{\min}$ and $d_{\max}$ can be set to 1 μm and 100 μm, respectively. The lower and upper limits of air gap depends mostly on the standard processes used to assemble the microgenerator. For a practical MEMS process, $g_{\min}$ and $g_{\max}$ are set to 50 and 500 μm, respectively. $V_{\max}$ is assumed to be 1000 V which is achievable if employing corona discharge method. Teflon PTFE is assumed to be the electret material used in this study, and hence, the dielectric strength is $E_0 = 155$ MV/m. The external load is assumed to vary from $R_{\min} = 1$ MΩ to $R_{\max} = 1$ GΩ. The frequency of interest, f_0, is assumed to be 20 Hz in this optimization. In addition, there is a need to evaluate C_p to include in the optimization. Given that C_p is due to fringing effects at the edges of electrodes which is directly proportional to the FEM capacitance at zero overlapping $C_{\min}$, we perform a numerical study for $C_{\min}$ at various effective gap spacing $d/\varepsilon_d + g$. The result plotted in Figure 12 shows only a slight variation of $C_{\min}$, especially at gap spacing below 250 μm. As a result, the variation of C_p is neglected in this optimization.

Figure 13 shows the output power generated by the microgenerator as the volume constrained by the dielectric and Paschen's breakdown voltages. The result of the optimization using a non-linear program solver shows that an optimal output power of 61.7 μW can be obtained when

$$\begin{cases} d & = 6.5\ \mu m \\ g & = 143\ \mu m \\ V_0 & = 1000\ V \\ R_L & = 765\ \text{M}\Omega \end{cases}. \tag{29}$$

This results in 4 times higher than the power generated by the non-optimal structure described in Table 2.

As expected, the optimal power generated by the microgenerator requires a balance between the electret thickness d, the air gap g and the potential V_0 to ensure no material failure or discharging of the electret occur. In this case, $d = 6.5$ μm, $g = 143$ μm and $V_0 = 1000$ V satisfy all the requirements and result in the highest output power. This,

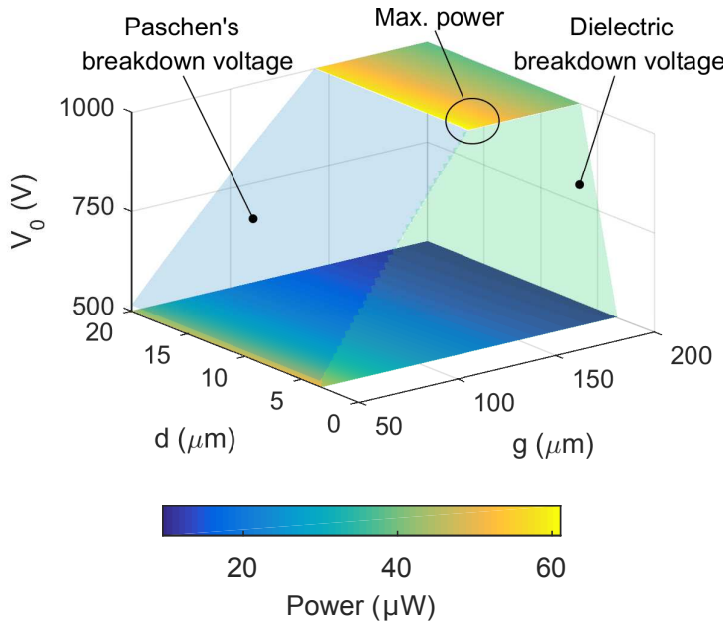

Figure 13. Output power generated by the electret-based microgenerator is plotted with respect to electret thickness d, air gap g and electret surface potential V_0 under a 2 mm peak-to-peak excitation at $f = 20$ Hz. Due to the Paschen's breakdown voltage presented as the transparent blue surface on the left and dielectric breakdown voltage presented as the transparent green surface on the right, a smaller d and g do not result in the highest output power. In this case, the maximum power is determined as 61.7 μW when d =6.5 μm, $g = 143$ μm and $V_0 = 1000$ V and $R_L = 765$ MΩ.

again, emphasizes the importances of breakdown effects when designing and fabricating electret-based microgenerators.

6 Conclusion

In summary, we successfully develop an analytical model for electret-based microgenerators excited under small sinusoidal vibrations. We also include the effect of parasitic capacitances and formulate a closed-form solution that accurately predicts the performance of practical microgenerators. The analytical model shows that the electrodynamics of the microgenerators are equivalent to a sawtooth-signal voltage in series with an internal resistance. The developed model is validated using FEM and numerical methods. The presented result shows a good agreement between the model and the conducted simulation. In addition, we employ the analytical model combined with voltage breakdown effects to investigate the importance of material properties when designing and optimizing electret-based microgenerators.

Acknowledgement

This work is supported by the Department of State Development: Collaboration Pathways Program - South Australia Government (CPP 39).

References

Asanuma, H., Oguchi, H., Hara, M., Yoshida, R. & Kuwano, H. (2013), 'Ferroelectric dipole electrets for output power enhancement in electrostatic vibration energy harvesters', *Applied Physics Letters* **103**(16), 162901.

Bartsch, U., Sander, C., Blattmann, M., Gaspar, J. & Paul, O. (2009), Influence of parasitic capacitances on the power output of electret-based energy harvesting generators, *in* 'Proc. PowerMEMS', pp. 332–335.

Boisseau, S., Despesse, G., Ricart, T., Defay, E. & Sylvestre, A. (2011), 'Cantilever-based electret energy harvesters', *Smart Materials and Structures* **20**(10), 105013.

Boisseau, S., Despesse, G. & Sylvestre, A. (2010), 'Optimization of an electret-based energy harvester', *Smart Materials and Structures* **19**(7), 075015.

Boland, J., Chao, Y.-H., Suzuki, Y. & Tai, Y. C. (2003), Micro electret power generator, *in* 'Proc. MEMS', pp. 538–541.

Chen, R. & Suzuki, Y. (2013), 'Suspended electrodes for reducing parasitic capacitance in electret energy harvesters', *Journal of Micromechanics and Microengineering* **23**(12), 125015.

Franco, S. (2002), *Design With Operational Amplifiers And Analog Integrated Circuits*, 3rd edn, McGraw-Hill, chapter 4, pp. 187–188.

Genter, S. & Paul, O. (2012), Parylene-C as an electret material for micro energy harvesting, *in* 'Proc. PowerMEMS', pp. 317–320.

Gradshteyn, I. S. & Ryzhik, I. M. (2014), *Table of integrals, series, and products*, Academic press, chapter 3, p. 318.

Graham, J. B., DeWar, H., Lai, N., Lowell, W. R. & Arce, S. M. (1990), 'Aspects of shark swimming performance determined using a large water tunnel', *Journal of Experimental Biology* **151**(1), 175–192.

Hirasaki, E., Moore, S. T., Raphan, T. & Cohen, B. (1999), 'Effects of walking velocity on vertical head and body movements during locomotion', *Experimental brain research* **127**(2), 117–130.

Husain, E. & Nema, R. S. (1982), 'Analysis of Paschen curves for air, N2 and SF6 using the Townsend breakdown equation', *IEEE Transactions on Electrical Insulation* **EI-17**(4), 350–353.

James, E., Tudor, M., Beeby, S., Harris, N., Glynne-Jones, P., Ross, J. & White, N. (2004), 'An investigation of self-powered systems for condition monitoring applications', *Sensors and Actuators A: Physical* **110**(1), 171–176.

Jefimenko, O. D. & Walker, D. K. (1978), 'Electrostatic current generator having a disk electret as an active element', *IEEE Transactions on Industry Applications* (6), 537–540.

Masaki, T., Sakurai, K., Yokoyama, T., Ikuta, M., Sameshima, H., Doi, M., Seki, T. & Oba, M. (2011), 'Power output enhancement of a vibration-driven electret generator for wireless sensor applications', *Journal of Micromechanics and Microengineering* **21**(10), 104004.

Meninger, S., Mur-Miranda, J. O., Amirtharajah, R., Chandrakasan, A. & Lang, J. H. (2001), 'Vibration-to-electric energy conversion', *IEEE Transactions on Very Large Scale Integration (VLSI) Systems* **9**(1), 64–76.

Nakano, J., Komori, K., Hattori, Y. & Suzuki, Y. (2015), MEMS rotational electret energy harvester for human motion, *in* 'Proc. PowerMEMS', p. 012052.

Naruse, Y., Matsubara, N., Mabuchi, K., Izumi, M. & Suzuki, S. (2009), 'Electrostatic micro power generation from low-frequency vibration such as human motion', *Journal of Micromechanics and Microengineering* **19**(9), 094002.

Romero, E., Warrington, R. O. & Neuman, M. R. (2009), Body motion for powering biomedical devices, *in* 'Proc. EMBS', IEEE, pp. 2752–2755.

Roundy, S. & Wright, P. K. (2004), 'A piezoelectric vibration based generator for wireless electronics', *Smart Materials and structures* **13**(5), 1131–1142.

Roundy, S., Wright, P. K. & Rabaey, J. (2003), 'A study of low level vibrations as a power source for wireless sensor nodes', *Computer communications* **26**(11), 1131–1144.

Smith, E. (2013), *Mechanical Engineer's Reference Book*, Elsevier Science, chapter 7, p. 7/126.

Sodano, H. A., Park, G. & Inman, D. (2004), 'Estimation of electric charge output for piezoelectric energy harvesting', *Strain* **40**(2), 49–58.

Tada, Y. (1986), 'Theoretical characteristics of generalized electret generator, using polymer film electrets', *IEEE transactions on electrical insulation* (3), 457–464.

Tada, Y. (1992), 'Experimental characteristics of electret generator, using polymer film electrets', *Japanese journal of applied physics* **31**(3R), 846.

Tsutsumino, T., Suzuki, Y., Kasagi, N., Kashiwagi, K. & Morizawa, Y. (2006), Micro seismic electret generator for energy harvesting, *in* 'Proc. PowerMEMS', pp. 279–282.

Tsutsumino, T., Suzuki, Y., Kasagi, N. & Sakane, Y. (2006), Seismic power generator using high-performance polymer electret, *in* 'Proc. MEMS', pp. 98–101.

Weisstein, E. W. (2002), 'Hypergeometric function.', From MathWorld - A Wolfram Web Resource. URL: http://mathworld.wolfram.com/HypergeometricFunction.html. Access on September 14th, 2016.

Williams, C. & Yates, R. B. (1996), 'Analysis of a micro-electric generator for microsystems', *Sensors and Actuators A: Physical* **52**(1), 8–11.

Yen, B. C. & Lang, J. H. (2006), 'A variable-capacitance vibration-to-electric energy harvester', *IEEE Transactions on Circuits and Systems I: Regular Papers* **53**(2), 288–295.

Zhou, Y., Apo, D. J. & Priya, S. (2013), 'Dual-phase self-biased magnetoelectric energy harvester', *Applied Physics Letters* **103**(19), 192909.